International Journal of Multiphase Flow 188 (2025) 105219

Contents lists available at ScienceDirect

International Journal of Multiphase Flow

journal homepage: www.elsevier.com/locate/ijmulflow

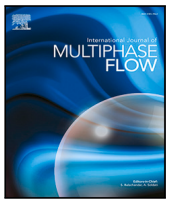

Research Paper

A new approach to unravel the lift force phenomenon of a single bubble rising in stagnant and sheared liquids

Mohammad Karimi Zand [a,b], Stefan Puttinger [b], Mahdi Saeedipour [b,*]

[a] K1-MET Metallurgical Competence Center, Stahlstraße 14, 4020 Linz, Austria
[b] Department of Particulate Flow Modelling, Johannes Kepler University, A-4040 Linz, Austria

ARTICLE INFO

Keywords:
Bubble dynamics
Bubble lift
Vorticity
Deformation
Interface-resolved simulation
Volume of fluid (VOF) method

ABSTRACT

The lateral distribution of bubbles rising in plumes is determined by the lift force induced on the bubbles. The lift force is exerted due to the presence of vorticity in the immediate vicinity of the bubble. Here, we have proposed a new approach to describe how the interface deformation governed by the surface tension force contributes to the vorticity generation near the bubble, subsequently leading to the lift force's emergence. Using the vorticity transport equation, we compute the vorticity generation rate due to the bubble deformation, and compare it to the bubble lateral acceleration, which is a representation of the lateral forces acting on the bubble. Using the interface-resolved volume of fluid (VOF) method, we have simulated single bubbles rising in both stagnant liquid, and under the influence of a background shear flow. Bubbles with different sizes were simulated inside various liquid media, corresponding to a wide range of Eotvos numbers ($0.55 < Eo < 5.96$) and Morton numbers ($-10.5 < Log\,Mo < -3.8$). Results disclose a consistent match between vorticity generation rate due to the bubble deformation and the lateral force induced on the bubble on both freely-rising condition and rising with presence of a background shear. This theory implies a physical interconnection between these phenomena which not only describes the zigzag movements of bubbles when rising freely, but also explains the direction change of bubble lateral migration in shear flows. The findings hold a direct implication in defining a universal lift force model for describing bubble lateral movements.

1. Introduction

Bubbly plumes and bubble columns are among the most important multiphase flows that are widely used directly in numerous industrial processes and applications. Examples include but are not limited to bubble column reactors, wastewater treatment, and metallurgical plants. One of the most important uses in metallurgical industries is the argon curtain bubbly plume used in steel production for delivering flotation of non-metallic inclusions (NMI) (Zhong et al., 2006). Therefore, in-depth understanding of bubbly plume characteristics such as bubble size, flow regime, bubble coalescence and breakup, and liquid mixing is essential to deliver a robust process outcome (Zhang and Taniguchi, 2000; Mirsandi et al., 2020). The behavior and flow regime of the bubble plume is dictated by a force called the lift force (Shu et al., 2019), therefore it is essential to have a thorough understanding and definition of the lift force to predict the radial void fraction and flow regime of the plume. The lift force is defined as perpendicular to the direction of bubbles movement trajectory, which is usually upwards under the influence of buoyancy force (Legendre and Magnaudet, 1998). According to previous studies, this lateral lift force is a result of a rotational background flow which the bubble is rising in Mudde (2005). Two of the most practical and fundamental cases that represent bubbles rising in a rotational flow are bubbly plumes in pipe flows, which generally have a Poiseuille velocity profile, and bubbles rising in a simple linear shear flow. In addition, the relative velocity between the bubble and the background flow also influences the lift force. The lift coefficient needs to be determined to calculate the value of the lift force acting on bubbles. A fundamental research on evaluation of the lift force was carried out by Tomiyama et al. (2002). They utilized a moving belt to create a simple linear shear flow in a viscous dominant liquid (mixture of water and glycerol), and analyzed the bubble rise path, focusing on lateral migration of bubbles with different diameters. They concluded that the lift force coefficient is primarily a function of bubble modified Eotvos number which itself is a function of bubble deformation. In summary, they observed that smaller bubbles always move away from the high background velocity in the shear flow and move towards the stationary wall, and larger bubbles move towards the regions that have higher background velocity i.e. towards the belt (Tomiyama et al., 2002). The lift coefficient for smaller bubbles is

* Corresponding author.
E-mail address: mahdi.saeedipour@jku.at (M. Saeedipour).

https://doi.org/10.1016/j.ijmultiphaseflow.2025.105219
Received 8 November 2024; Received in revised form 24 January 2025; Accepted 8 March 2025
Available online 17 March 2025

defined as positive, and for larger bubbles is defined as negative. In their formulation of lift force and lift coefficient, they lumped the effect of background shear and bubble wake, but no explicit investigation of the effect of bubble wake was done. It should be noted that since their experiment was conducted in a viscous dominant regime, the bubble path did not show considerable path instability and zigzag movement which makes it reasonable to focus less on the effect of bubble wake. In another notable research on determining bubble lift coefficient (Aoyama et al., 2017) studied the bubble dynamics in a low Morton number regime ($-6.6 \leq Log\,\mathrm{Mo} \leq -3.2$) using the same setup of Tomiyama et al. (2002). They concluded that the lift force coefficient cannot be solely described by a single property related to the bubble or the liquid, and confirmed the reversal of the sign of lift coefficient with bubble size increase as reported by Tomiyama et al. (2002).

In the case of a small bubble that keeps its spherical shape for high enough Reynolds numbers ($Re > 100$), generation of the lift force is caused by the distortion of the background vorticity (present in the shear flow) due to the presence of the bubble. This tilting and stretching of the streamwise vorticity causes a concentration of vorticity very close to the bubble, downstream of the bubble interface. High values of the Reynolds number indicates that the flow could be regarded as inviscid. This is the reason that the actual values of the lift coefficient in the work of Tomiyama et al. (2002) for the case of smaller bubbles come close to the analytical value given by Auton (1987) for a spherical bubble present in an inviscid shear flow, $C_L = 0.5$ (Legendre and Magnaudet, 1998). This mechanism was first introduced by Lighthill (1956), and Auton (1987) calculated the value of the lift force caused by this mechanism. Therefore, it is called the Lighthill or L-mechanism (Hidman et al., 2022). When a spherical bubble is rising in a low Reynolds number shear flow, the lift force is still induced due to the presence of vorticity at the immediate vicinity of the bubble (Legendre and Magnaudet, 1998). A background shear flow causes asymmetric advection of the shear-free generated vorticity and its asymmetric distribution around the bubble. This is called the Saffman mechanism. Saffman derived the analytical solution of the lift force induced on a rigid spherical particle in a viscous flow (Saffman, 1965), which later on was used to explain the lift force induced on a spherical bubble in a low Reynolds number liquid (Legendre and Magnaudet, 1998). In this case, the lift coefficient of the spherical bubble is a function of bubble Reynolds number and the dimensionless shear rate, and generally has positive values. If the bubble has a high Reynolds number it will have a lift force coefficient of $C_L = 0.75$ in the beginning of its rise which will later on decrease to the famous $C_L = 0.5$ after reaching a steady state.

Bubble movement in liquids like water which have relatively low viscosity and/or high surface tension is a lot more complex, especially when the bubble size becomes larger. Bubbles rising in surface tension-inertial force dominant regimes exhibit zigzag and spiraling trajectories with or without the presence of a background shear flow (Lee and Lee, 2020; Mougin and Magnaudet, 2002). A fundamental study carried out in a non-viscous dominant liquid is the study of Ziegenhein et al. (2018). They investigated air bubbles in water (low Morton number system) with a background shear induced by an adjacent bubble plume, and proposed a lift model as a function of the modified Eotvos number. In a more recent study using the same experimental setup, Hessenkemper et al. (2021) measured the bubble and liquid velocity simultaneously, and included two effects in their improved lift force coefficient: (i) shear rate as a function of dimensionless shear rate (Sr) and Reynolds number (Legendre and Magnaudet, 1998), and (ii) bubble deformation as a function of modified Eotvos number. Reversal of lift force for larger bubbles was also reported in these works, indicating that sign change of the lift coefficient happens essentially due to bubble deformation and its subsequent vorticity generation.

According to Adoua et al. (2009), the sign change of the lift coefficient happens due to higher vorticity generation on the bubble interface with increasing bubble deformation. With increasing bubble size, bubbles tend to deform from the spherical shape, Especially in low Morton number liquids. They concluded that the tilting and stretching of the vorticity generated at the bubble surface due to the shear-free condition of the gas-liquid interface creates a pair of counter rotating vortices downstream of the bubble, which causes the emergence of the lift force and a sign change in the presence of a background shear. Other related studies such as Mougin and Magnaudet (2002) and Magnaudet and Mougin (2007) have connected the oscillations in the bubble rise path to the bubble deformation and an increase in surface vorticity. They also reported that the rise path starts becoming unstable when a pair of counter rotating vortices appear behind the bubble. These vortices are rooted in the advection of the surface generated vorticity. In these studies, bubble shape was kept fixed and a deformation factor was prescribed for the bubbles. This means that the bubbles simulated in these studies where symmetrical ellipsoids having larger horizontal axis.

Among all of the lift formulations available in the literature, only a few have considered the vorticity at the immediate vicinity of the bubble in their lift coefficient formulations, and almost all of the DNS works have used bubbles having rigid shapes. Recently, in the work of Hayashi et al. (2020), it has been proven that the lift force acting on a bubble is essentially a result of the vorticity on the bubble surface. Just as it has already been proven previously in the literature that the drag force relates to the layer of vorticity residing on the bubble surface. Hayashi et al. (2020) used the functional form of the maximum vorticity production at the bubble interface provided in the work of Magnaudet and Mougin (2007), which correlates with deformation, and the functional form of drag coefficient formulation (Moore, 1965). They explained the relation of this drag coefficient to the maximum vorticity on the bubble surface, and subsequently to the bubble deformation in a viscous dominant flow regime. Then, using a function that they defined which relates the lift coefficient to the drag coefficient, they deduced a formulation for the lift force which is a function of the surface vorticity and bubble deformation. Using the same strategy, Hayashi et al. (2021) and Lee and Lee (2020) derived the lift coefficient as a function of surface vorticity for the surface tension dominant flow regime. In the work of van der Linden (2022), they have computed the magnitude of the boundary layer vorticity concentrated in a thin layer on the bubble surface i.e. one mesh cell thickness, and its compliance with the lateral forces imposed on the bubble in two different reference frames. Then, they have defined a new lift force coefficient based on the relation between this vorticity and the calculated lateral lift force. Their calculation, however, resulted in only positive values for the vorticity around the bubble. In contrast, the lateral lift forces obtained from their DNS revealed an oscillating pattern with both negative and positive values, which could not be effectively diagnosed. Hidman et al. (2022) in a comprehensive work investigated the vorticity values in a volume control around the bubble, and defined lift force coefficients for every single mechanism mentioned in their paper. Subburaj et al. (2023) also defined a lift coefficient based on the vorticity of the background shear and the gas volume fraction distribution using CFD-DEM simulation iterations and comparing the data to their experiments.

After a thorough search of the literature, it is evident that an investigation into the bubble lateral movement based on the general vorticity transport equation is lacking. More specifically, a study that ponders on vorticity generation rate by the bubble deformation, and its connection to the lift force is missing in the literature. Most of the aforementioned research that consider the bubble-generated vorticity in their lift coefficients use models and functions that determine this bubble-generated vorticity by estimations. Other methods that use spatial integration on mesh cells inherently have errors regarding accurate vorticity layer thickness that may cause acute errors in the vorticity and lift calculations. In addition, when averaging the vorticity in the mesh cells, it is not possible to differentiate between surface-generated vorticity, and the vorticity of the flow field caused by the liquid displacement due to bubble non-linear dynamics, or the vorticity

of the background shear and its advection around the bubble. In this study, we explain the bubble lateral movement based on the transport equation of vorticity, especially based on the surface tension term, while the bubble shape is free to change and oscillate. First, bubbles rising freely in different liquid media are analyzed and the relation between deformation-induced vorticity production term and lateral acceleration is investigated. Doing so will shed light on the forces applied on the bubble which are perpendicular to the rise path. Next, bubbles rising in a background shear flow are analyzed from the same perspective, with the insights achieved from the freely-rising cases. This will help to unravel a general mechanism for the lift force on the bubble based on the concept of vorticity, and independent of the liquid properties. A universal description like this is essential for developing closure force models in the context of Eulerian-Lagrangian methods that enable efficient simulations of bubbly plumes.

2. Theory and research methodology

2.1. Theoretical concept

To describe the hydrodynamics of single bubble motion in liquid it is a common practice to consider the governing equations of immiscible liquid-gas flows with one-fluid formulation. This comprises the continuity and Navier–Stokes equations for the mixture:

$$\frac{\partial \rho}{\partial t} + \nabla \cdot (\rho \boldsymbol{u}) = 0 \tag{1}$$

$$\frac{\partial (\rho \boldsymbol{u})}{\partial t} + \nabla \cdot (\rho \boldsymbol{u}\boldsymbol{u}) = -\nabla p + \nabla \cdot \boldsymbol{\tau} + \mathbf{F}_i + \mathbf{F}_\sigma \tag{2}$$

where $\boldsymbol{u}$ is the fluid velocity shared between the liquid and gas phases, p is the pressure, and $\boldsymbol{\tau}$ is the stress tensor which for a Newtonian fluid with no compressibility effect is defined as $\boldsymbol{\tau} = \mu\left(\nabla \boldsymbol{u} + \nabla \boldsymbol{u}^{\top}\right)$. $\mathbf{F}_i$ is the sum of external and conservative forces e.g. the gravity, and $\mathbf{F}_\sigma$ is the surface tension force induced on the gas-liquid interface. In these equations, the material properties are assumed as arithmetic mean between the ones of each phase using a weighted volume average phase indicator function, α. Therefore, the density and viscosity read $\rho = \alpha\rho_1 + (1-\alpha)\rho_2$ and $\mu = \alpha\mu_1 + (1-\alpha)\mu_2$, respectively. This entails an additional transport equation to track and determine this indicator function.

$$\frac{\partial \alpha}{\partial t} + \nabla \cdot (\alpha \boldsymbol{u}) = 0 \tag{3}$$

Tracking the interface between liquid and gas is also essential for determining surface tension force by the Continuous Surface Force (CSF) method (Brackbill et al., 1992). This approach defines the surface tension as $\mathbf{F}_\sigma = \sigma\kappa\,\hat{\mathbf{n}}\delta_s$, and connects it to the derivatives of phase indicator function because $\hat{\mathbf{n}} = \frac{\nabla\alpha}{|\nabla\alpha|}$ is the interface normal vector and $\kappa = -\nabla \cdot \hat{\mathbf{n}}$ is the interface local curvature.

While this set of equations is able to describe the hydrodynamics of any liquid-gas flow, in order to delve deep into the of lift force phenomenon based on the concept of vorticity and provide a physical understanding of the underlying mechanisms, a perception of the lift force formulation is still needed.

By examining the general formulation for lift force on a moving object in fluid e.g. bubble (Auton, 1987):

$$F_L = -C_L \rho_L V_b (\mathbf{u_b} - \mathbf{v}) \cdot (\nabla \times \mathbf{v}) \tag{4}$$

where $\mathbf{u_b}$ is the bubble velocity, and $\mathbf{v}$ is the surrounding liquid velocity, it is evident that the magnitude of the lift force is proportional to the vorticity of the rotational flow. According to previous studies, in a given reference frame (Fig. 1), the z-component of the vorticity field corresponds to the lateral lift force imposed on the bubble in x-direction that is rising upwards towards y-direction. Applying this understanding derived from previous studies, the z-component of vorticity generated by the bubble deformation forces is correlated with lateral bubble acceleration, which is the representative of the lift force in x-direction,

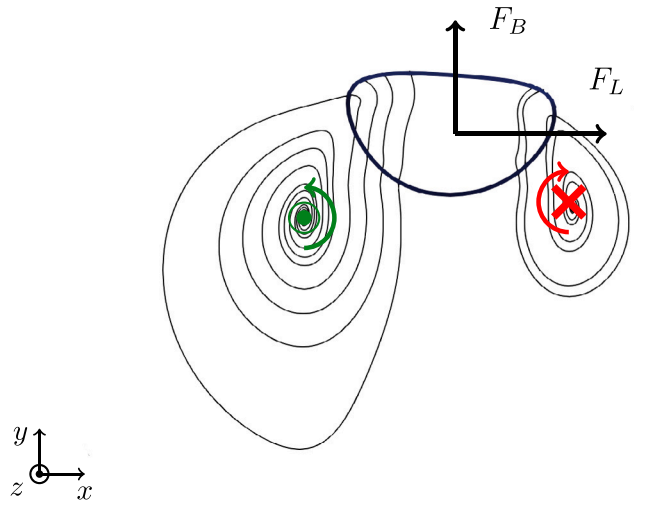

Fig. 1. Definition of lift force (F_L) imposed on the bubble perpendicular to the buoyancy force (F_B) in xy-plane, and the flow streamlines past a deformed rising bubble. Vortical structures generated by the bubble movement explain positive flow rotation ($\omega_z > 0$) (green), and negative flow rotation ($\omega_z < 0$) (red). (For interpretation of the references to color in this figure legend, the reader is referred to the web version of this article.)

to find the interconnection between them. It has to be emphasized that our analysis of the theory remains valid regardless of the chosen dimensional orientation. This means that the analysis and the results are consistent whether we observe the bubble from xy- or zy-plane. The physical interconnection between the vorticity and the tallying lateral acceleration remains the same.

Due to higher surface tension in lower Morton number liquids, vorticity generation on bubble surface is higher, and lower liquid viscosity results in less damping effect on this vorticity generation, and wobbliness of the bubble. This can be apprehended by taking a look at the general transport equation of vorticity ($\boldsymbol{\omega} = \nabla \times \boldsymbol{u}$) in multiphase flows which includes an interface between a gas and liquid phase (Magnaudet and Mercier, 2020)

$$\frac{D\boldsymbol{\omega}}{Dt} = \underbrace{(\boldsymbol{\omega} \cdot \nabla)\boldsymbol{u}}_{\text{vortex stretching}} + \underbrace{\nabla \times \left(-\frac{\nabla p}{\rho}\right)}_{\text{baroclinic effect}} + \underbrace{\nabla \times \left(\frac{1}{\rho}\nabla \cdot \tau\right)}_{\text{viscous dissipation}} + \underbrace{\nabla \times (\frac{1}{\rho}\mathbf{F}_\sigma)}_{\text{surface tension}} \tag{5}$$

The first term on the right hand side, which is the vortex stretching term, is responsible for advecting the vorticity downstream of the bubble movement. This downstream advection of the vorticity results in generation of wakes behind the bubble. The second term represents the vorticity generation due to misalignment of density and pressure gradients present in the flow. The third term on the right hand side is the curl of the stress tensor, which represents the diffusive term. This term which generally possesses negative values, is responsible for the dissipation of vorticity by viscous forces. The last term is the curl of the surface tension force that exists at the gas-liquid interface (Magnaudet and Mercier, 2020), which after expansion, contains terms that vanish due to the alignment between the density gradient vector ($\nabla\rho$) and the volume fraction gradient vector ($\nabla\alpha$) as well as the fact that the curl of a gradient of a scalar is zero. For a complete explanation of this derivation, we refer to Hasslberger et al. (2018). Finally, this term reduces to:

$$\boldsymbol{\omega}_s = \frac{\sigma}{\rho}\nabla\kappa \times \nabla\alpha \tag{6}$$

Obviously, this vorticity generation mechanism only relates to the misalignment between the gradient vectors of the local interface curvature and volume fraction (Hasslberger et al., 2018; Saeedipour, 2023). In other words, this vector quantity describes the rate of vorticity

variation by the geometrical change and deformation of the bubble surface. Thus, in low Morton number liquids, when the bubble shape deforms and heavily deviates from the perfect spherical shape, this term becomes non-zero, and the generation of vorticity at the immediate vicinity of the bubble should not be neglected. Only when the bubble retains its perfectly spherical shape (or close to sphere) these effects can be disregarded. Similar to other terms in Eq. (5), $\dot{\boldsymbol{\omega}}_s$ has the physical unit of [T^{-2}], and when integrated component-wise along with the bubble interface, it determines the instantaneous contribution of interface geometry to vorticity production or destruction in that direction. Thus, its correlation with the rate of change in the bubble lateral motion i.e. acceleration could constitute a direct physical connection between bubble deformation and the lift force.

To realize this connection, we adopt an integration algorithm along with the bubble interface and calculate Eq. (6) in a subdomain near the bubble surface. What is meant by subdomain here, is the thin layer of gas-liquid interface. We analyze the subdomain-averaged values of this term in the direction perpendicular to the bubble rising path i.e. $\langle \dot{\omega}_{s,z} \rangle = \frac{1}{\mathcal{V}} \int_{\mathcal{V}} \dot{\boldsymbol{\omega}}_{\mathbf{s},z} \, \mathrm{d}v$, and base our discussion on its temporal variation in comparison with the lateral acceleration of the bubble ($\mathbf{a}_x = \frac{\mathrm{d}\mathbf{u}_{\mathbf{b},x}}{\mathrm{d}t}$). The latter is computed by tracking the velocity of the bubble center of mass ($\mathbf{u_b}$) in time, and holds the physical unit of [L T^{-2}]. It is needless to mention that this theoretical concept can be tested by analyzing accurate geometrical details of three-dimensional bubble rising motion that could be obtained by high-fidelity numerical simulations (such as VOF method) or 3D reconstruction of bubble shape from high resolution experimental images.

2.2. Interface-resolved numerical simulation

In this study, we have obtained the necessary data for analysis of rising bubbles by conducting interface-resolved numerical simulations using the volume of fluid (VOF) method that solves the discretized forms of Eqs. (1) to (3) using the finite volume method. We have simulated single bubbles with different Eotvos numbers rising in stagnant and sheared liquids with different Morton numbers. For these simulations, we have utilized the geometrical VOF solver in open-source software OpenFOAM known as isoAdvector method (Roenby et al., 2016), that uses a two-step reconstruction-propagation operation based on the iso-surface of the volume fraction. This method is implemented in the solver `interIsoFoam`. Particularly, in the context of rising gas bubble simulation, the study of Gamet et al. (2020) has shown that this approach provides a very accurate curvature calculation and significantly reduces the spurious currents. In addition, for some cases that are explained later, we also employed the algebraic VOF solver of `interFoam`. Through appropriate discretization and providing sufficient spatial resolution, these solvers can perform reliable interface-resolved simulations, as demonstrated in our previous studies (Saeedipour et al., 2021; Mahmoudi et al., 2024). The transient terms in the equations are discretized using a first-order implicit (Euler) scheme in both of these solvers. The convection term in the momentum equation is discretized with a Gauss linear scheme. For the convection of the phase fractions in the VOF equation, the Gauss vanLeer scheme is employed. Lastly, the diffusion term is discretized using the Gauss Linear Corrected scheme. For calculating the volume fluxes and reconstructing the interface, `interIsoFoam` uses the Piecewise Linear Interface Calculation (PLIC), which eliminates the spurious currents sometimes created at the interface (Meier et al., 2002). Nevertheless, to conduct numerical simulation for a range of bubble sizes with sufficiently long rising path, the spatial resolution remains a limiting factor. Particularly, for bubbles with diameter of 2 mm or smaller, a large number of fine grid cells were to be used that would have made the simulations computationally unaffordable. Additionally, the adaptive mesh refinement (AMR) technique that is provided in OpenFOAM software is not fully compatible with the isoAdvector interface detection techniques in `interIsoFoam` solver. To the authors best knowledge, there is no simple solution to bypass the errors of AMR when used in `interIsoFoam`. Thus, for the cases that small bubble sizes were simulated, `interFoam` combined with AMR was used.

2.3. Simulation setup

The numerical domain defined in this study is a 3D rectangular box with $L \times L \times H = 40 \text{ mm} \times 40 \text{ mm} \times 400 \text{ mm}$ as depicted in Fig. 2. The bubble is free to rise in the domain, meaning no axisymmetric boundary condition was used in the simulations, and the gas-liquid interface is free to change its shape and oscillate. For the boundary conditions, free slip is selected for the walls to reduce the effect of wall presence. A pressure outlet boundary condition is selected for the top wall of the rectangular box.

The domain is discretized with isotropic hexahedral mesh cells with uniform size throughout the domain. According to the quantitative benchmarks provided by Adelsberger et al. (2014) for 3D simulations of bubbles and droplets rising under the influence of buoyancy force in liquid media, OpenFOAM is able to capture the bubble dynamics in terms of shape deformation and terminal rise velocity with a minimum mesh resolution of 16 cells per bubble diameter. In this study, a minimum mesh resolution of 25 mesh cells per bubble diameter is used ($D_b/\delta = 25$) when simulating on uniform grids with `interIsoFoam`. In the cases that AMR is employed for simulating the smaller bubble, the domain mesh size has an initial scaling of 4 with bubble diameter. Then, with three levels of mesh refinement inside and around the bubble interface, the mesh resolution $D_b/\delta = 32$ is achieved in the area surrounding the bubble. Since in the beginning of the simulation the bubble is introduced as a sphere, a test of sphericity, originally suggested in the work of Wadell (1935), was performed. The result of this test showed an error value of less than 0.4% which proves that these OpenFOAM simulations can be regarded as a good representation of a sphere. Furthermore, a mesh dependence study was conducted (not presented here) to examine the accuracy of the AMR for the small bubble based on the terminal rise velocity, and the results for the $D_b/\delta = 32$ show terminal rise velocity values almost exactly the same as it has been reported in the book of Clift et al. (1978). In the cases that the effect of shear flow is studied, the same configuration presented in Fig. 2 is further adapted with a linear shear defined from the bottom plane, and the simulation is run until the whole domain has a fully developed shear profile. The shear rate induced on the domain in all of the cases is defined as 6.25 s^{-1} throughout the whole domain.

According to the literature, there are four different mechanisms and flow regimes that dictate the bubble lateral movement in a shear flow. These mechanisms are categorized by the bubble Eotvos number ($Eo = g(\rho_l - \rho_b)L_C^2/\sigma$) and Galilei number ($Ga = \rho_l \sqrt{g L_C} L_C/\mu_l$) (Hidman et al., 2022), where ρ_l and ρ_b are the liquid and bubble densities, respectively. Also, L_C is the bubble characteristic length which is the spherical equivalent diameter, σ is the liquid surface tension, and μ_l is the liquid viscosity. In this study, the ranges of Eo and Ga are defined by the variation of liquid properties such that all of the aforementioned mechanisms are included into the analysis. The operating conditions that correspond to these four mechanisms are defined as EL1, EH1, EL2, and EH2. As discussed formerly in this paper, an increase in liquid viscosity (decrease in Ga number), results in less bubble shape oscillation. To provide a broader image, two additional cases, EL3 and EH3, were also defined with lower Ga numbers for both bubble sizes in which bubbles show little to no shape oscillation. A summary of the simulation cases are listed in Table 1:

The simulation cases studied in this paper are also shown in the so-called Grace diagram (Clift et al., 1978) in Fig. 3. As the cases defined here cover a wide range of operating conditions from low Morton number regimes like air/water operating conditions, to more viscous dominant and high Morton number flow regimes, we aim to bridge the gap between different studies available in the literature, and provide base for a general understanding for the lift force.

To provide further validation, we have also calculated the lift force coefficients of the simulated bubbles similar to the method used in Lee and Lee (2020) using the bubble trajectories. We compare these values with the data and correlations for different conditions investigated in

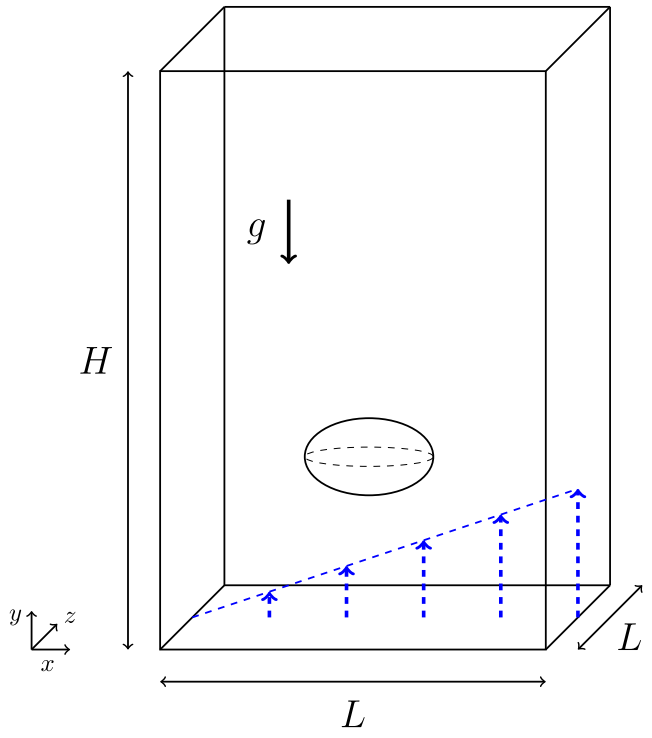

Fig. 2. Schematic view of the computational domain with the bubble in the center of the box subject to buoyancy-driven rising motion. For cases that are simulated with the presence of background shear, the shear flow profile is shown in blue dashed lines. (For interpretation of the references to color in this figure legend, the reader is referred to the web version of this article.)

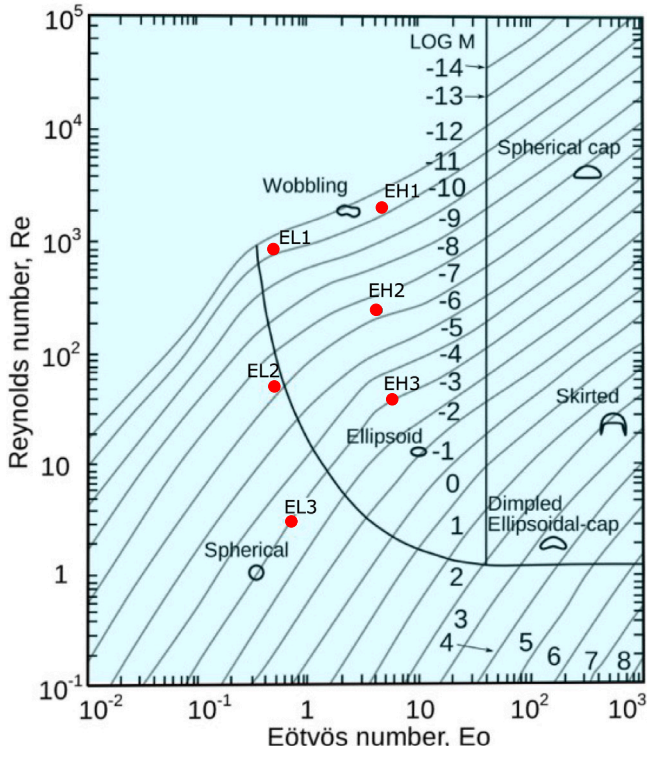

Fig. 3. Demonstration of the simulation cases on the Grace-diagram. The diagram, retrieved and adapted from Clift et al. (1978), highlights the simulation cases as red markers. (For interpretation of the references to color in this figure legend, the reader is referred to the web version of this article.)

Table 1
The description of simulation cases with the range of bubble dimensionless numbers of Eo and Ga. In all simulated cases, the surface tension coefficient is kept constant with the value $\sigma = 0.071$ N/m. Reynolds number is calculated for cases with background shear.

	d_b (mm)	μ_l (Pa s)	Eo	Ga	Re	*Log* Mo
EL1	2	1.0518×10^{-3}	0.55	266.3	380.3	−10.47
EH1	6	1.0518×10^{-3}	4.97	1383	1547.2	−10.47
EL2	2	1.0518×10^{-2}	0.61	29.30	29.97	−6.51
EH2	6	1.0518×10^{-2}	5.47	152.24	171.27	−6.51
EL3	2	5.25×10^{-2}	0.66	6.65	6.6	−3.82
EH3	6	5.25×10^{-2}	5.96	34.58	35.3	−3.82

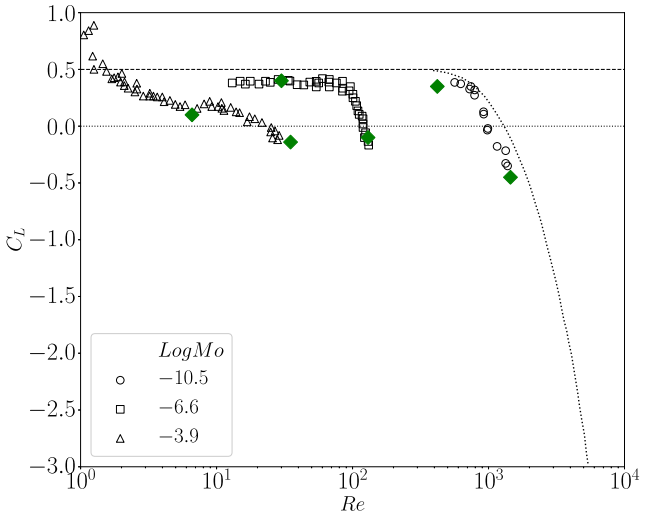

Fig. 4. Comparison of the lift coefficients with the data and correlation from literature. The data are retrieved from the corresponding plots published in Hayashi et al. (2021) using graph data extraction: green markers denote predicted values by the simulation cases in the present study (Table 1), empty markers denote the lift coefficients obtained by different experimental data. Lowest Morton numbers represent air–water experiments of Hessenkemper et al. (2021) and the dotted line is the lift coefficient correlation derived for air–water systems from Hayashi et al. (2021). (For interpretation of the references to color in this figure legend, the reader is referred to the web version of this article.)

the literature. Fig. 4 presents this comparison with the extracted data from the works of Hayashi et al. (2021) and Hessenkemper et al. (2021) for the same Morton numbers in our study. This comparison reveals a very good agreement with the experimental data and provides a verification for the simulation data in this study.

3. Results and discussion

3.1. Freely rising bubbles

At first, the results of freely rising bubbles are presented and analyzed in detail. We base our discussion on two sets of results for all the simulation cases: (i) bubble rise path in the xy-plane, and (ii) the vorticity/acceleration plots that follows the theoretical concept presented in sub- Section 2.1. For the former, we track the bubble center of mass, and for the latter, the bubble lateral acceleration ($\mathbf{a}_x$) is computed by the time derivative of the lateral velocity of bubble center of mass. The bubble lateral velocity is extracted by integrating the velocity components from the finite volume cells containing gas phase i.e. $\alpha \neq 0$, and reads $\mathbf{u_b}_{,x} = \frac{\int_V \alpha \mathbf{u}_x \, \mathrm{d}v}{\int_V \alpha \, \mathrm{d}v}$. Furthermore, the deformation-induced vorticity rate, $\dot{\omega}_{s,z}$, is computed locally for each finite volume cell based on Eq. (6), and then integrated for the cells around the bubble. It has to be noted that for the sake of comparison both quantities are normalized by the maximum values obtained for the larger bubble with the same properties in the air/water system, and result in $\langle \dot{\omega}_{s,z} \rangle^*$

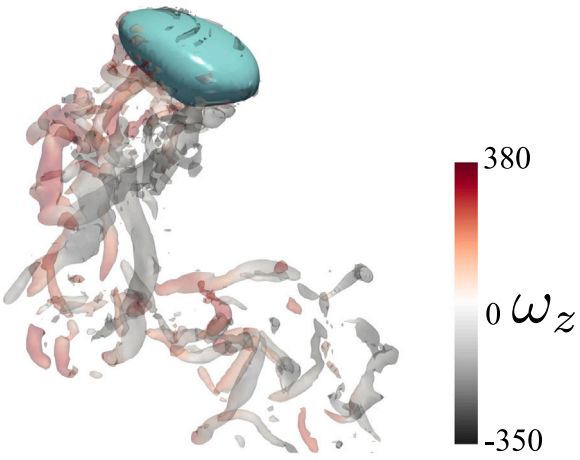

Fig. 5. An instantaneous 3D snapshot of a air bubble freely rising in stagnant water corresponding to the case EH1. The bubble is visualized by iso-surfaces of $\alpha = 0.5$, with vortical structures downstream of the bubble colored by the vorticity component in z-direction. (For interpretation of the references to color in this figure legend, the reader is referred to the web version of this article.)

and $\mathbf{a}_x^*$ that are compared with each other for every simulated case. This makes the comparison more meaningful as the effect of bubble size is also included in the amplitude of the oscillations. An instantaneous 3D snapshot of the bubble rising throughout the stagnant liquid, generating vortical structures in its rise path is presented in Fig. 5.

Fig. 6 presents the detailed results for EL1 and EH1 which are the cases of a small and a large bubble with characteristic diameters of 2 mm and 6 mm, respectively, in water. As Fig. 6(a) demonstrates, the bubble reveals slight oscillation in its rising path through the liquid. Vorticity generation rate due to deformation, plotted in Fig. 6(b), also appears to have oscillating values around zero. It is evident that the oscillation pattern of the lateral acceleration follows the same pattern of the vorticity generation rate. Fig. 6(c) & (d) demonstrate the same plots for the EH1. In these plots bubble zigzag movement is also prevalent, with the amplitude of the zig-zags being larger than EL1. Fig. 6(d) illustrates the strong correlation between vorticity generation rate and the lateral acceleration of the bubble, with much higher amplitudes compared to those of EL1.

One observation worth mentioning is that even though the acceleration follows the same pattern of $\langle \dot{\omega}_{s,z} \rangle$, it seems to have a dilatory behavior. Later, we will demonstrate that this observation holds true across each vorticity and acceleration plot presented in this paper. This delay between $\dot{\omega}_s$ and acceleration show that first the vorticity is being generated by the act of surface deformation, and then this is turned into the lateral acceleration i.e. lift force. Although this trend was also mentioned in the work of van der Linden (2022) as a possible reason for the mismatch in their force model verification, their additional results on the temporal variation of the lift force indicate the opposite behavior, probably because they calculated the vorticity magnitude ($\|\boldsymbol{\omega}\|$) around the bubble and not its production rate i.e. $\langle \dot{\boldsymbol{\omega}} \rangle$. Conversely, our approach examines vorticity production in the vicinity of the bubble by emphasizing its rate, which reveals a meaningful physical interconnection to the acceleration, as both quantities scale with s^{-2}.

As explained in Eq. (6), deformation-induced vorticity generation rate is due to the misalignment between curvature gradient and volume fraction gradient. Since the surface tension coefficient of the liquid in all cases is similar, the larger magnitude of $\langle \dot{\omega}_{s,z} \rangle$ in EH1 implies a higher degree of bubble deformation that is attributed to the increased bubble size. This is also confirmed by the bubble surface area plot and instantaneous snapshots of the 3D bubble shapes provided in Fig. 7. The bubble surface area is extracted from the volume fraction fields as $\mathbf{A_b} = \int_{\mathcal{V}} \delta_s \, \mathrm{d}v$, with δ_s being Dirac delta function approximated by $\|\nabla\alpha\|$ (Saeedipour and Schneiderbauer, 2022), and is normalized by the surface area value at the beginning of the simulation, $\mathbf{A_0} = \pi d_b^2$, which is the analytical value for a sphere. Since for the same volume, the sphere has the smallest surface area compared to any other arbitrary geometrical shape, an increase in the $\mathbf{A_b}$ means deforming from the initial spherical shape. The bubble shape in EL1 at most of the times is close to a simple, slightly damped, spheroid, with small wobblings and deformings from this state. This can be considered as less deformation compared with the bubble shape of EH1 which shows a more arbitrary ellipsoidal shape with high amplitudes of shape deformation and wobbling behavior.

In EL2 and EH2, for the same bubble sizes of 2 mm and 6 mm, the viscosity of the surrounding liquid is increased resulting in $Log\,\mathrm{Mo} = -6.5$, and corresponds to a liquid mixture of 60% glycerol/water solution. According to the Grace diagram in Fig. 3, it is expected that the bubble in EL2 would have a spherical shape, and the bubble in EH2 would have less wobbling behavior. The rise path trajectory of EL2 presented in Fig. 8(a) shows infinitesimal zigzag movement. Vorticity generation rate and bubble lateral acceleration presented in Fig. 8(b) both show values close to zero, and the overall plot shows a flat line. This is due to the fact that the bubble retains its spherical shape along the rise path as a consequence of small volume (low Eo), and the high viscosity of the liquid that is keeping the bubble confined in its spherical shape. A 3D snapshot of the bubble shape is provided in Fig. 8(a).

For the larger bubble in the same liquid viscosity, case EH2 shows a different rise path compared to EL2. It shows steady rising behavior at first, and then shows zigzag movement of the bubble at almost halfway through the domain. By looking at the vorticity generation and lateral acceleration plots, it can be seen that also in the beginning vorticity generation shows a flat line with values equal to zero. After the bubble gains enough momentum due to buoyancy force, it starts to wobble and generate vorticity. A brief look at the bubble shape throughout the rise path in Fig. 8(c), can also prove this point: the lateral force imposed on the bubble indicated by the lateral acceleration is initiated by the start of the vorticity generation due to deformation.

Increasing the liquid viscosity to even higher values around $\mu_l = 0.05$ to simulate a 80% mixture of glycerol/water solution with $Log\,\mathrm{Mo} = -3.8$ results in even more damping of the surface deformation and wobbliness of the bubble. According to the Grace diagram, with this viscous dominant flow not only the smaller bubble in EL3, but also the larger bubble in EH3 is expected to have very low wobbling behavior. The bubble rise path and vorticity/lateral acceleration plots for the smaller bubble in EL3 is almost exactly the same as plots for EL2, and therefore are not provided here to prevent repetition. In EL2, the lateral bubble acceleration plots show values close to zero. This is also aligned with the $\langle \dot{\omega}_{s,z} \rangle^*$ that yields nearly zero values at all times, illustrating a flat line. However, in EH3, the bubble shape is a symmetrical oblate spheroid with almost no shape oscillation and wobbling as displayed in Fig. 9(a). This symmetrical shape results in equal values for $\dot{\omega}_{s,z}$ with opposite signs at regions on bubble surface with high curvature gradient near the bubble tips, thus the integration of the local vorticity rates results in zero (i.e. $\langle \dot{\omega}_{s,z} \rangle \approx 0$). This puts the bubble in a force equilibrium state, meaning no lateral movement would be observed. In contrast, in EH2 even though the bubble shape is close to an oblate spheroid, but after a while it starts to oscillate and deform from the symmetrical spheroid state, and this is the reason that the average vorticity generated by the interface has non zero values compared to EH3, and the lateral force imposed on the bubble has oscillating values causing the bubble to have zigzag movements throughout its rise path.

3.2. Bubbles rising in the presence of background shear

In the remainder of the paper, we investigate the bubble rise behavior in the presence of a background shear. The aim of this investigation

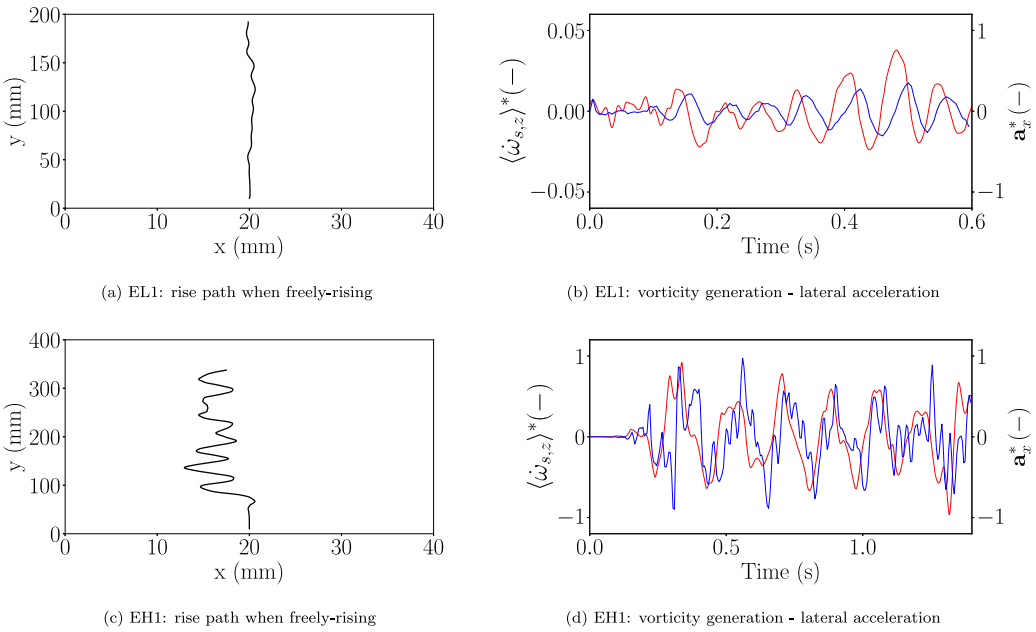

(a) EL1: rise path when freely-rising

(b) EL1: vorticity generation - lateral acceleration

(c) EH1: rise path when freely-rising

(d) EH1: vorticity generation - lateral acceleration

Fig. 6. Analysis of the cases EL1 (top row) and EH1 (bottom row) when freely-rising: bubble rise path in xy-plane (left column), and temporal variation of normalized vorticity rate $\langle \dot{\omega}_{s,z} \rangle^*$ (—) and lateral acceleration $\mathbf{a}_x^*$ (—) (right column).

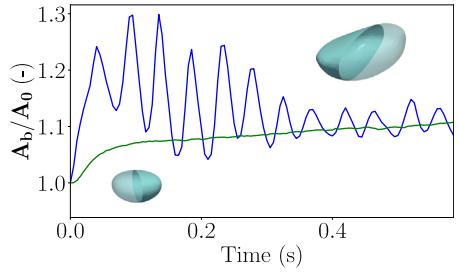

Fig. 7. Normalized bubble surface area for EL1 (—) and EH1 (—), and random instantaneous snapshots of bubble shapes.

is to analyze the effect of shear on the observed compliance between lateral acceleration deformation-induced vorticity generation, and if it still explains the transverse migration of the bubbles even in the presence of the shear. Therefore, all the simulated cases are once again simulated in a domain with a linear shear profile as schematically shown in Fig. 2.

It is discussed in the introduction that when bubble is able to keep an ideal spherical shape, the shear flow causes the bubble to travel to the regions of lower velocity (e.g. pipe wall in the case of bubbly pipe flow.). In these cases, whether the bubble is moving through a high Morton number liquid (Saffman, 1965; Legendre and Magnaudet, 1998), or an ideal inviscid flow with low Morton number (Lighthill, 1956; Auton, 1987), the lift force is derived analytically. These analytical expressions are also validated by the abundant experimental and numerical DNS studies in the literature. Recent studies have defined lift models that generally are composed of two main terms; i.e. $F_L = f(Sr) - f(Def)$ (Hessenkemper et al., 2021; Lee and Lee, 2020). The first term corresponds to the effect of the background shear on the lateral movement on the bubble, which causes the bubble to move to the regions with lower background velocity. The second term is a function of bubble deformation, and reverts the sign of the lift force. By increasing bubble deformation, the value of this function also increases, thus it will contribute more to the total calculated lift force imposed on the bubble.

In our simulations, the cases that the bubble has an ideal spherical shape are EL2 and EL3. As a representative, the bubble rise path of EL2 is shown in Fig. 10(a). The bubble path shows a linear rise tilted towards the left side of the domain, which is the region with lower background velocity. In Fig. 10(b), it is evident that vorticity generation due to deformation has little to no effect on the lateral forces imposed on the bubble, as $\langle \dot{\omega}_{s,z} \rangle$ yields values close to zero. Thus, the only mechanism that induces a force on the bubble perpendicular to the rise path is the vorticity caused by the background shear flow.

As mentioned earlier, with a decrease in the liquid Morton number in EL1, the bubble becomes prone to more shape oscillation and deformation, resulting in more vorticity generation by the deformation. By examining the bubble rise path in Fig. 10(c), it is evident that the bubble still goes towards the region of the flow that has lower velocity, but the trajectory is not as linear as the EL2 and EL3. Consequently, the plots in Fig. 10(d) show oscillating values for $\langle \dot{\omega}_{s,z} \rangle$. The overall trend of the bubble lateral acceleration follows the same pattern of the vorticity generation, having the same extrema points, but it appears to have a downshift towards negative values. This implies that in this case the vorticity generation on the bubble surface influences the bubble acceleration, but the dominant mechanism is the lift force that is exerted on the bubble by the shear flow, causing it to traverse to the left side of the domain, and having negative overall value for acceleration in x-direction.

With an increase in Eo number with increasing bubble size, $\dot{\boldsymbol{\omega}}_s$ increases and therefore, it will have a greater influence on the bubble lateral acceleration. It is observed in Fig. 11 that in the cases of EH1 and EH2 the bubble trajectory reveals oscillatory movement towards the region of higher background velocity, which is inline with previous studies. The $\langle \dot{\omega}_{s,z} \rangle$ and bubble lateral acceleration show alignments in terms of oscillation pattern and magnitude. Again, this alignment of lateral acceleration with vorticity generation rate indicates that the lateral force induced on the bubble is primarily influenced by $\dot{\boldsymbol{\omega}}_s$. EH1 shows more chaotic behavior due to higher shape oscillation because of the lower Morton number of the liquid.

Nonetheless, alignment between lateral acceleration and $\langle \dot{\omega}_{s,z} \rangle$ does not elucidate the direction change of bubble lateral migration in the presence of the shear. In order to shed light on this change of behavior with larger bubbles and clarify whether it is the shape oscillation that is causing this transverse migration, the case with highest liquid viscosity (EH3) is also simulated in the presence of background shear. The bubble rise path presented in Fig. 12(a) still displays bubble lateral

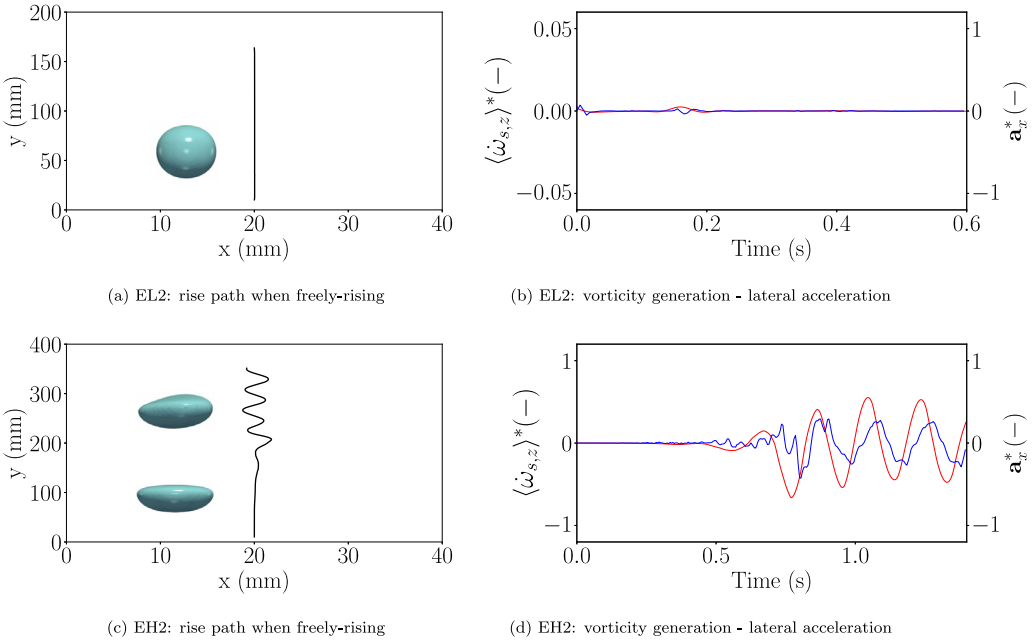

(a) EL2: rise path when freely-rising

(b) EL2: vorticity generation - lateral acceleration

(c) EH2: rise path when freely-rising

(d) EH2: vorticity generation - lateral acceleration

Fig. 8. Analysis of the cases EL2 (top row) and EH2 (bottom row) when freely-rising: bubble rise path in xy-plane (left column), and temporal variation of normalized vorticity rate $\langle \dot{\omega}_{s,z} \rangle^*$ (—) and lateral acceleration $\mathbf{a}_x^*$ (—) (right column).

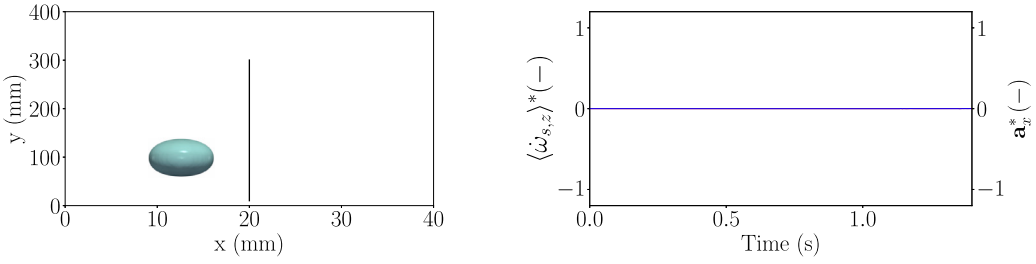

(a) EH3: rise path when freely-rising

(b) EH3: Vorticity generation - lateral acceleration

Fig. 9. Analysis of the case EH3 when freely-rising: (a) bubble rise path in xy-plane, and (b) comparison of $\langle \dot{\omega}_{s,z} \rangle^*$ (—) and $\mathbf{a}_x^*$ (—).

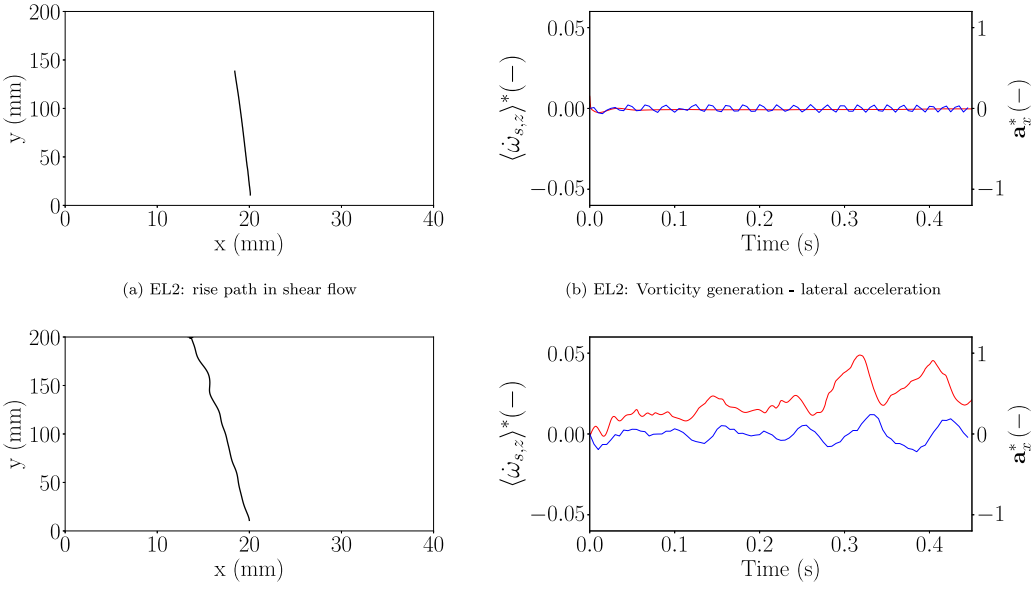

(a) EL2: rise path in shear flow

(b) EL2: Vorticity generation - lateral acceleration

(c) EL1: rise path in shear flow

(d) EL1: Vorticity generation - lateral acceleration

Fig. 10. Analysis of the cases EL1 (bottom row) and EL2 (top row) in the presence of background shear: bubble rise path in xy-plane (left column), and temporal variation of normalized vorticity rate $\langle \dot{\omega}_{s,z} \rangle^*$ (—) and lateral acceleration $\mathbf{a}_x^*$ (—) (right column).

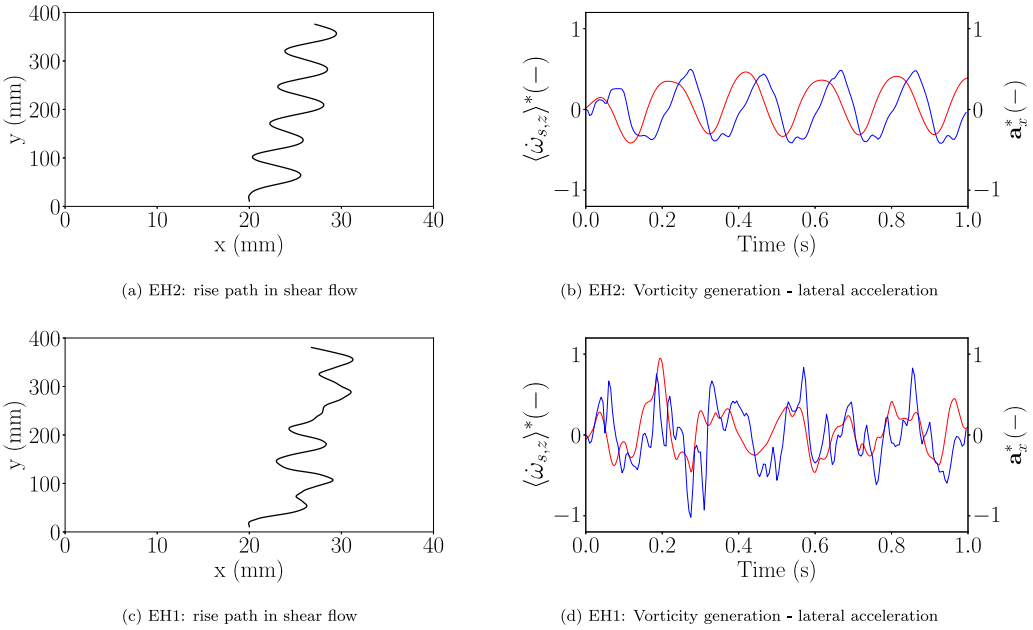

(a) EH2: rise path in shear flow

(b) EH2: Vorticity generation - lateral acceleration

(c) EH1: rise path in shear flow

(d) EH1: Vorticity generation - lateral acceleration

Fig. 11. Analysis of the cases EH1 (bottom row) and EH2 (top row) in the presence of background shear: bubble rise path in xy-plane (left column), and temporal variation of normalized vorticity rate $\langle \dot{\omega}_{s,z} \rangle^*$ (—) and lateral acceleration $\mathbf{a}_x^*$ (—) (right column).

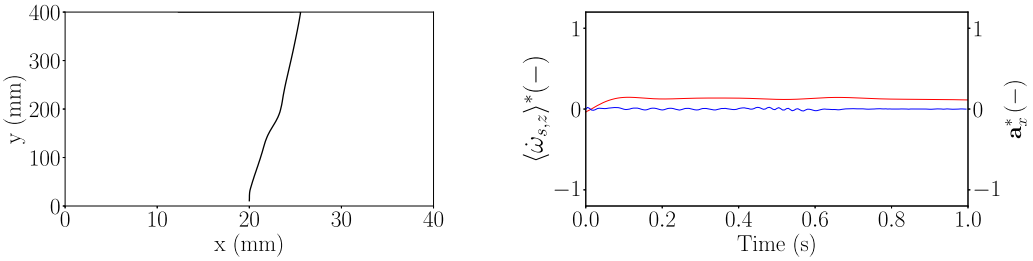

(a) Rise path in shear flow

(b) Vorticity generation - lateral acceleration

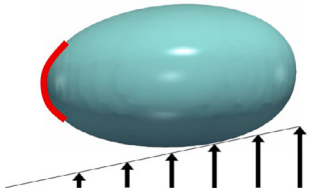

(c) 3D bubble shape

Fig. 12. Analysis of the case EH3 in the presence of background shear: (a) Bubble rise path in xy-plane, (b) comparison of $\langle \dot{\omega}_{s,z} \rangle^*$ (—) and lateral acceleration $\mathbf{a}_x^*$ (—), and (c) instantaneous 3D bubble shape with background velocity vectors schematically visualized by straight arrows.

migration towards region with higher background velocity, but the path shows almost no zig-zag movement, implying the fact that in this case also the bubble has almost no wobbling behavior. Previously in the case of freely rising, this bubble revealed no shape oscillation which resulted in $\langle \dot{\omega}_{s,z} \rangle \approx 0$. But, a close examination of vorticity rate given in Fig. 12(b) indicates that in the presence of a background shear, the net value of $\langle \dot{\omega}_{s,z} \rangle$ is not zero anymore and shows a constant positive rate over time. Therefore, it can be inferred that in the presence of a background shear and very high viscosity, the bubble does not keep a symmetrical shape anymore. This is also evident in the 3D snapshot of the bubble presented in Fig. 12(c).

Fig. 12(c) further shows that the bubble has more curvature in its side pointed towards the region of the flow with lower background velocity, resulting in higher $\nabla\kappa$. According to Eq. (5), a higher curvature gradient results in higher $\dot{\boldsymbol{\omega}}_s$. This higher rate of vorticity generation on one side of the bubble disrupts the equilibrium state that was present in the case of EH3 rising in quiescent liquid, and generates a non-zero lift force that pushes the bubble towards the opposite direction. The bubble's tendency to develop a higher curvature in the areas of lower background velocity can be explained by Bernoulli's law: regions with lower flow velocity generally experience higher pressure, which increases the surface curvature of the bubble on that side. This observation sheds light on the direction change of the large deforming bubbles when migrating in the presence of the shear flow. It can be hypothesized that the presence of the shear flow could induce asymmetrical deformation in these bubbles regardless of the flow Morton number, and this higher vorticity generation is actually happening for the previous EH1 and EH2 cases. The difference in positive and

negative vorticity production rate by the bubble deformation is small relative to the high overall vorticity production rate in lower Morton number cases, therefore it is likely masked by the scale of the plots in Fig. 11(b) and (d). But the influence of this asymmetric vorticity production rate adds up cumulatively over time, which causes the bubble to travel to the right side. Nevertheless, this explanation still requires further quantification and proof, which will be the focus of future studies. Besides, this behavior had been suspected by previous researchers without a quantified proof, probably because of not observing bubble behavior in less chaotic regimes which happen in higher Morton number regimes (van der Linden, 2022).

4. Conclusions

In this research, the lateral and zig-zag motions of single bubble rising in stagnant liquid or under the influence of a background shear flow are analyzed by theory and direct numerical simulations. Accordingly, a universal framework for understanding the lift force on the bubble is sought by focusing on the relationship between vorticity generation due to bubble surface deformation and the lateral acceleration of the bubbles.

For this purpose, various bubble flow regimes and liquid properties with and without background shear were analyzed, covering a range of dimensionless numbers: $0.55 < \mathrm{Eo} < 5.96$ and $6.65 < \mathrm{Ga} < 1383$, corresponding to $-10.5 < Log\,\mathrm{Mo} < -3.8$, which includes the operating conditions investigated in the works of Tomiyama et al. (2002), Hayashi et al. (2021), and Hessenkemper et al. (2021). Interface-resolved VOF simulations of these cases were carried out and the relevant simulation data were extracted and analyzed. A compliance between the vorticity generation due to bubble deformation and the lateral acceleration, which is a representation of the lift forces imposed on the bubble is observed in all the simulations: first the vorticity is generated by the bubble deformation, and then this deposited vorticity on the interfacial region turns into a lateral force. When bubbles are rising freely in a stagnant liquid, the amplitude of zig-zag movements and lateral acceleration corresponds to the amplitude of the vorticity generation. Furthermore, this mechanism not only holds for the lift on freely-rising bubbles, but also describes the lateral motion of bubbles in different size in interaction with the imposed vorticity from the background shear flow. When vorticity generation due to deformation is low for spherical bubbles (small bubbles) the vorticity of the background shear flow is the dominating mechanism that dictates bubble lateral movements. By increasing vorticity generation due to deformation which happens with increasing bubble deformation (larger bubbles), this term overrules the shear flow vorticity and dictates the bubble lateral migration. Even though similar behavior has been reported in the literature, (e.g. Adoua et al. (2009)) it is worth mentioning that previous work had been using fixed-shaped bubbles in their studies. This will essentially eliminate the contribution of the vorticity generation rate due to bubble deformation which has been the focus of this paper. In addition, most of the previous DNS studies have been using rigid symmetric ellipsoids for bubble shapes. The results of this study suggest that symmetric ellipsoids exhibit a zero-total vorticity generation rate, while asymmetry in the bubble shape appears to contribute to deviations from equilibrium in vorticity generation and causes a non-zero lift force emergence. This physical interconnection has not been discussed previously in the literature, especially in modeling of the lateral lift force, and supports the arguments on the effect of the delay between vorticity and lift force in previous modeling attempts (van der Linden, 2022). Nevertheless, this aspect still requires further quantification in future studies.

The present work provides a deeper understanding on the role of vorticity generation by the bubble. The theoretical framework proposed in this study is unified among all dimensionless numbers that characterize the bubble flow regimes, and the findings pave the path towards a more accurate definition of the lift force based on this principal physical attribute of the bubble regardless of the liquid properties. We plan to verify these findings also experimentally by analyzing 3D shape reconstruction of bubbles in the future work. Furthermore, as a part of an ongoing investigation on the up-scaling simulation methodology for bubbly flows, the present findings could contribute to development of new universal lift model in the context of Eulerian-Lagrangian simulations. Our future work will focus on the development, implementation and validation of such a closure model for the lift force, and its overall performance in the prediction of hydrodynamics and heterogeneity of the bubbly plumes will be validated against experimental measurement obtained by the tomographic PIV method.

CRediT authorship contribution statement

Mohammad Karimi Zand: Writing – original draft, Visualization, Software, Methodology, Investigation, Formal analysis, Data curation, Conceptualization. **Stefan Puttinger:** Validation, Software, Resources, Investigation, Funding acquisition. **Mahdi Saeedipour:** Writing – review & editing, Supervision, Software, Project administration, Methodology, Investigation, Funding acquisition, Formal analysis, Conceptualization.

Declaration of competing interest

The authors declare the following financial interests/personal relationships which may be considered as potential competing interests: Mahdi Saeedipour reports financial support was provided by K1-MET GmbH. Mahdi Saeedipour reports a relationship with Austrian Research Promotion Agency that includes: funding grants. If there are other authors, they declare that they have no known competing financial interests or personal relationships that could have appeared to influence the work reported in this paper.

Acknowledgments

The authors gratefully acknowledge the funding support of K1-MET GmbH metallurgical competence center. The research program of the K1-MET competence center was supported by COMET (Competence Center for Excellent Technologies), the Austrian program for competence centers. COMET was funded by the Federal Ministry for Climate Action, Environment, Energy, Mobility, Innovation and Technology, the Federal Ministry for Digital and Economic Affairs, the Federal States of Upper Austria, Tyrol and Styria, as well as the Styrian Business Promotion Agency (SFG). In addition to the public funding from COMET, this research project was partially financed by the industrial partners (voestalpine Stahl Linz GmbH, voestalpine Stahl Donawitz GmbH, and RHI Magnesita GmbH).

Data availability

Data will be made available on request.

References

Adelsberger, J., Esser, P., Griebel, M., Groß, S., Klitz, M., Rüttgers, A., 2014. 3D incompressible two-phase flow benchmark computations for rising droplets. In: Proceedings of the 11th World Congress on Computational Mechanics (WCCM XI), Barcelona, Spain.

Adoua, R., Legendre, D., Magnaudet, J., 2009. Reversal of the lift force on an oblate bubble in a weakly viscous linear shear flow. J. Fluid Mech. 628, 23–41.

Aoyama, S., Hayashi, K., Hosokawa, S., Lucas, D., Tomiyama, A., 2017. Lift force acting on single bubbles in linear shear flows. Int. J. Multiph. Flow 96, 113–122.

Auton, T.R., 1987. The lift force on a spherical body in a rotational flow. J. Fluid Mech. 183, 199–218.

Brackbill, J., Kothe, D., Zemach, C., 1992. A continuum method for modeling surface tension. J. Comput. Phys. 100 (2), 335–354.

Clift, R.R., Grace, J.R., Weber, M.E., 1978. Bubbles, Drops, and Particles. Academic Press, p. 380.

Gamet, L., Scala, M., Roenby, J., Scheufler, H., Pierson, J.L., 2020. Validation of volume-of-fluid OpenFOAM® isoAdvector solvers using single bubble benchmarks. Comput. Fluids 213, 104722.
Hasslberger, J., Klein, M., Chakraborty, N., 2018. Flow topologies in bubble-induced turbulence: a direct numerical simulation analysis. J. Fluid Mech. 857, 270–290.
Hayashi, K., Hessenkemper, H., Lucas, D., Legendre, D., Tomiyama, A., 2021. Scaling of lift reversal of deformed bubbles in air-water systems. Int. J. Multiph. Flow 142.
Hayashi, K., Legendre, D., Tomiyama, A., 2020. Lift coefficients of clean ellipsoidal bubbles in linear shear flows. Int. J. Multiph. Flow 129, 103350.
Hessenkemper, H., Ziegenhein, T., Rzehak, R., Lucas, D., Tomiyama, A., 2021. Lift force coefficient of ellipsoidal single bubbles in water. Int. J. Multiph. Flow 138, 103587.
Hidman, N., Ström, H., Sasic, S., Sardina, G., 2022. The lift force on deformable and freely moving bubbles in linear shear flows. J. Fluid Mech. 952, A34.
Lee, W., Lee, J.Y., 2020. Experiment and modeling of lift force acting on single high Reynolds number bubbles rising in linear shear flow. Exp. Therm. Fluid Sci. 115, 110085.
Legendre, D., Magnaudet, J., 1998. The lift force on a spherical bubble in a viscous linear shear flow. J. Fluid Mech. 368, 81–126.
Lighthill, M.J., 1956. Drift. J. Fluid Mech. 1 (1), 31–53.
van der Linden, T., 2022. DNS Investigation on the Lift Force of Single Bubbles. (Master's thesis). Eindhoven University of Technology.
Magnaudet, J., Mercier, M.J., 2020. Particles, drops, and bubbles moving across sharp interfaces and stratified layers. Annu. Rev. Fluid Mech. 52, 61–91.
Magnaudet, J., Mougin, G., 2007. Wake instability of a fixed spheroidal bubble. J. Fluid Mech. 572, 311–337.
Mahmoudi, S., Saeedipour, M., Hlawitschka, M., 2024. Bubble dynamics under the influence of the Marangoni force induced by a stratified field of contamination. Exp. Comput. Multiph. Flow 6, 353–364.
Meier, M., Yadigaroglu, G., Smith, B.L., 2002. A novel technique for including surface tension in PLIC-VOF methods. Eur. J. Mech. B Fluids 21, 61–73.
Mirsandi, H., Baltussen, M.W., Peters, E.A., van Odyck, D.E., van Oord, J., van der Plas, D., Kuipers, J.A., 2020. Numerical simulations of bubble formation in liquid metal. Int. J. Multiph. Flow 131, 103363.
Moore, D.W., 1965. The velocity of rise of distorted gas bubbles in a liquid of small viscosity. J. Fluid Mech. 23 (4), 749–766.
Mougin, G., Magnaudet, J., 2002. Path instability of a rising bubble. Phys. Rev. Lett. 88, 4.
Mudde, R.F., 2005. Gravity-driven bubbly flows. Annu. Rev. Fluid Mech. 37, 393–423.
Roenby, J., Bredmose, H., Jasak, H., 2016. A computational method for sharp interface advection. R. Soc. Open Sci. 3, 160405.
Saeedipour, M., 2023. An enstrophy-based analysis of the turbulence-interface interactions across the scales. Int. J. Multiph. Flow 164, 104449.
Saeedipour, M., Schneiderbauer, S., 2022. Toward a universal description of multiphase turbulence phenomena based on the vorticity transport equation. Phys. Fluids 34, 073317.
Saeedipour, M., Vincent, S., Estivalezes, J.L., 2021. Toward a fully resolved volume of fluid simulation of the phase inversion problem. Acta Mech. 232, 2695–2714.
Saffman, P.G., 1965. The lift on a small sphere in a slow shear flow. J. Fluid Mech. 22, 385–400.
Shu, S., Vidal, D., Bertrand, F., Chaouki, J., 2019. Multiscale multiphase phenomena in bubble column reactors: A review. Renew. Energy 141, 613–631.
Subburaj, R., Tang, Y., Deen, N.G., 2023. An improved lift model for Euler-Lagrange simulations of bubble columns. Chem. Eng. Sci. 265, 118182.
Tomiyama, A., Tamai, H., Zun, I., Hosokawa, S., 2002. Transverse migration of single bubbles in simple shear rows. Chem. Eng. Sci. 57, 1849–1858.
Wadell, H., 1935. Volume, shape, and roundness of quartz particles. J. Geol. 43 (3), 250–280.
Zhang, L., Taniguchi, S., 2000. Fundamentals of inclusion removal from liquid steel by bubble flotation. Int. Mater. Rev. 45, 59–82.
Zhong, L., Li, L., Wang, B., Jiang, M., Zhu, L., Zhang, L., Chen, R., 2006. Water modelling experiments of argon bubbling curtain in a slab continuous casting tundish. Steel Res. Int. 77, 103–106.
Ziegenhein, T., Tomiyama, A., Lucas, D., 2018. A new measuring concept to determine the lift force for distorted bubbles in low Morton number system: Results for air/water. Int. J. Multiph. Flow 108, 11–24.